crystals

MDPI

Article

Synthesis of Nanocrystalline Mn-Doped Bi_2Te_3 Thin Films via Magnetron Sputtering

Joshua Bibby [1], Angadjit Singh [1], Emily Heppell [1,2,3], Jack Bollard [1,2], Barat Achinuq [1,4], Sarah J. Haigh [5], Gerrit van der Laan [2] and Thorsten Hesjedal [1,*]

1 Clarendon Laboratory, Department of Physics, University of Oxford, Oxford OX1 3PU, UK; joshua.bibby@physics.ox.ac.uk (J.B.); angadjitsingh@hotmail.com (A.S.); emily.heppell@physics.ox.ac.uk (E.H.); jack.bollard@physics.ox.ac.uk (J.B.); bqachinuq@lbl.gov (B.A.)
2 Diamond Light Source, Harwell Science and Innovation Campus, Didcot OX11 0DE, UK; gerrit.vanderlaan@diamond.ac.uk
3 ISIS, Rutherford Appleton Laboratory, Harwell Science and Innovation Campus, Didcot OX11 0QX, UK
4 Advanced Light Source, Lawrence Berkeley National Laboratory, Berkeley, CA 94720, USA
5 Department of Materials, University of Manchester, Manchester M13 9PL, UK; sarah.haigh@manchester.ac.uk
* Correspondence: thorsten.hesjedal@physics.ox.ac.uk

Abstract: This study reports the structural and magnetic properties of Mn-doped Bi_2Te_3 thin films grown by magnetron sputtering. The films exhibit a ferromagnetic response that depends on the Mn doping concentration, as revealed by X-ray magnetic circular dichroism measurements. At an Mn concentration of ∼6.0%, a magnetic moment of $(3.48 \pm 0.25)\,\mu_B$/Mn was determined. Structural analysis indicated the presence of a secondary $MnTe_x$ phase, which complicates the interpretation of the magnetic properties. Additionally, the incorporation of Mn ions within the van der Waals gap and substitutional doping on Bi sites contributes to the observed complex magnetic properties. Intriguingly, a decrease in magnetic moment per Mn was observed with increasing Mn concentration, which is consistent with the formation of the intrinsic magnetic topological insulator $MnBi_2Te_4$.

Keywords: Mn-doped Bi_2Te_3; magnetic topological insulator; nanocrystalline topological insulator; magnetron sputtering; X-ray magnetic circular dichroism

check for updates

Academic Editor: Zaoli Zhang

Received: 4 December 2024
Revised: 31 December 2024
Accepted: 4 January 2025
Published: 7 January 2025

Citation: Bibby, J.; Singh, A.; Heppell, E.; Bollard, J.; Achinuq, B.; Haigh, S.J.; van der Laan, G.; Hesjedal, T. Synthesis of Nanocrystalline Mn-Doped Bi_2Te_3 Thin Films via Magnetron Sputtering. *Crystals* **2025**, *15*, 54. https://doi.org/10.3390/cryst15010054

Copyright: © 2025 by the authors. Licensee MDPI, Basel, Switzerland. This article is an open access article distributed under the terms and conditions of the Creative Commons Attribution (CC BY) license (https://creativecommons.org/licenses/by/4.0/).

1. Introduction

Topological insulators (TIs) such as Bi_2Te_3 have attracted the attention of the condensed matter physics community due to their topologically protected surface states, which result in rather unique electronic properties [1–5]. For applications in spintronics, however, these materials must break time-reversal symmetry (TRS) to induce a bandgap at the Dirac point, giving rise to phenomena such as the quantum anomalous Hall effect [6]. TRS breaking is typically achieved by introducing ferromagnetic order into the TI via transition metal doping [7]. This process induces an exchange interaction between the surface states and the spontaneous magnetization, leading to the formation of a small exchange gap [8]. To date, ferromagnetic doping has been successfully demonstrated in single crystals and molecular beam epitaxy (MBE)-grown thin films of various TIs. Elements such as Mn [9–19], Cr [20–25], Fe [25–29], and V [21,24,30] have all been explored as magnetic dopants, yielding promising results.

Despite these advancements, fully realizing the topological properties of TIs remains challenging, largely due to their bulk electronic properties [31]. Intrinsic defects introduce high bulk conductivity, often dwarfing the desired topological surface states [20]. Efforts

to eliminate these defects in ultra-pure systems are ongoing, but progress has been slow, prompting alternative approaches. One such strategy involves the use of nanocrystalline films, where grain sizes are optimized to suppress bulk conduction by essentially eliminating the bulk while maintaining the surface states [32,33]. This approach aligns well with the characteristics of magnetron sputtering, yielding granular material with tunable grain sizes controlled via the growth conditions.

In this work, we investigate Mn-doped Bi_2Te_3, one of the first TIs shown to exhibit TRS breaking [9]. From bulk Bi_2Te_3 bulk crystals, it is known that Mn doping induces ferromagnetic order at Mn concentrations of 2% (substituting for Bi), with a Curie temperature (T_C) in the range of 9–12 K [9]. Angle-resolved photoemission spectroscopy (ARPES) studies of MBE-grown Mn:Bi_2Te_3 thin films have further demonstrated a bandgap opening at the Dirac point, accompanied by a higher reported T_C of 45 K [34]. This study aims to explore the structural, magnetic, and topological properties of nanocrystalline Mn:Bi_2Te_3 films, utilizing magnetron sputtering as a scalable and industry-compatible deposition method to optimize film quality and grain size. We begin with a discussion of the growth methods employed to synthesize Mn-doped Bi_2Te_3 thin films. The results of structural analysis are then presented, focusing on the distribution of the Mn dopant within the Bi_2Te_3 crystal structure. Following the structural analysis, the magnetic properties of the films are explored through superconducting quantum interference device (SQUID) magnetometry and X-ray magnetic circular dichroism (XMCD). The paper concludes with a discussion of the relationship between Mn concentration, magnetic ordering, and structural features.

2. Materials and Methods

2.1. Thin Film Growth

Mn-doped Bi_2Te_3 films were grown on $10 \times 10\,mm^2$ $Al_2O_3(0001)$ substrates with a thickness of 430 µm using magnetron sputtering. Prior to deposition, the substrates were ultrasonically cleaned in acetone, isopropanol, and deionized water. The substrates were then placed in the deposition chamber, which had a base pressure of 2×10^{-8} mbar. For film deposition, 2″ sputter targets of Bi_2Te_3 (99.999% purity), Mn (99.9% purity), and Al (99.9% purity) were used. A well established two-step growth process was employed to fabricate the Mn:Bi_2Te_3 films [35]. First, a nucleation layer with a thickness of ∼1–2 nm was deposited at 200 °C using a sputtering power of 30 W, a deposition rate of ∼0.32 nm/s, and a growth pressure of 1.2×10^{-2} mbar. This was followed by deposition of the main layer at an elevated substrate temperature of 250 °C while maintaining the same deposition parameters. The main layer was grown to an equivalent thickness, typically of 25 nm of Bi_2Te_3, with the additional Mn flux contributing further to the total film thickness.

Doping was achieved via co-sputtering of Mn and Bi_2Te_3, with the Mn sputtering power ranging from 1 to 8 W. Two methods were employed to control the incorporation of Mn, namely, continuous co-sputtering and pulsed co-sputtering [36]. Given the growth rate ratio of Mn to Bi_2Te_3 (∼0.0057 vs. 0.0105 $nm\,s^{-1}\,W^{-1}$), pulsed co-sputtering involved periodically opening and closing the Mn shutter to achieve lower Mn concentrations. While this approach could result in alternating layers with varying Mn density, the known high mobility of Mn at the elevated growth temperature of 250 °C together with the relatively rough surface morphology and the low growth rate was expected to even out this effect, leading to a uniform Mn distribution throughout the film [37]. Additionally, the elevated temperature was anticipated to allow for Mn diffusion into the seed layer, effectively merging it with the main layer. To prevent oxidation, a 3–4 nm layer of amorphous Al was deposited, which naturally oxidizes in air to form a protective AlO_x layer. The Al layer was deposited at room temperature to minimize the risk of interfacial reactions with the underlying ferromagnetic film. Deposition was performed at a low power of 10 W

with a controlled deposition rate of 0.0373 nm/s, ensuring a uniform and stable coating. The elemental composition of the films was determined using energy-dispersive X-ray spectroscopy (EDS) (AZtec EDS, Oxford Instruments, High Wycombe, UK) in a scanning electron microscope (SEM) (JSM-6610LV, JEOL, Tokyo, Japan). Due to the low Mn content in some samples, precise Mn quantification was challenging; thus, the calibration relied on the two highest-doped samples. While SEM-EDS can be less reliable for thin films, particularly for elements that are present in small concentrations, potential errors were minimized by performing extended scans and taking measurements at multiple sites on the same film across different magnifications.

2.2. Structural Characterization

Structural analysis of the films was performed on an X-ray diffractometer (SmartLab II, Rigaku, Tokyo, Japan) using Cu Kα radiation. The system was configured with a parallel beam setup employing incident optics consisting of a 2.5° Soller slit, a 5 mm horizontal slit, and a 1 mm vertical slit. After diffraction, the beam passed through a Kβ filter and a 2.5° Soller slit before reaching the detector, which was positioned 300 mm from the sample. Measurements were conducted over a 2θ range of 5–80°.

The X-ray diffraction (XRD) data allowed for the calculation of Mn dopant concentration by measuring the shifts of the (00l) peak and determining changes in the lattice parameters induced by Mn incorporation. However, common out-of-plane XRD does not allow for the detection of secondary phases that are oriented differently with respect to the film's surface normal. To detect these phases, grazing-incidence XRD (GI-XRD) was employed. For GI-XRD, we utilized the same experimental setup as the standard XRD measurements but with the incident angle fixed at 4°. This allowed for the identification of any secondary phases formed during growth that might have been missed by the *c*-plane diffraction measurements.

Reciprocal space mapping (RSM) was also performed using two approaches. The first method utilized the same optical setup as the XRD measurements. To observe changes in reciprocal space due to Mn doping, this involved a sweep in ω and $2\theta/\omega$ around the (006) peak, which was the most intense (00l) peak. Additionally, asymmetric RSM was conducted to investigate off-axis peaks and gain insight into secondary phase formation within the films. This method employed the same instrument but with the diffracted beam optics removed, allowing the detector to operate in 2D mode. Measurements were taken over a parameter space spanning $-5°$ to 65° in χ and 0° to 100° in 2θ. This approach enabled the confirmation of secondary phase compositions by exploring regions of reciprocal space outside the *c*-plane.

The morphology of the films was analyzed using atomic force microscopy (AFM) in tapping mode (Nanoscope III), with the primary goal of assessing the grain size and distribution along with the surface roughness.

2.3. Electron Microscopy

To complement the XRD and surface morphology measurements, cross-sectional transmission electron microscopy (TEM) specimens were prepared using focused ion beam (FIB) milling (Nova 200 NanoLab, FEI, Hillsboro, OR, USA). Prior to FIB processing, a protective carbon layer was thermally evaporated onto the film outside of the FIB chamber. To further protect the film from Ga-ion implantation and beam damage during milling, sacrificial AuPd and Pt layers were deposited using the FIB system's electron and ion beams. Bright-field (BF) scanning transmission electron microscopy (STEM) images and EDS elemental maps of the samples were recorded using a latest-generation S/TEM (Talos

F200A, ThermoFisher, Waltham, MA, USA) equipped with Super-X EDS detectors and a 4k CMOS TEM camera (CETA, ThermoFisher, Waltham, MA, USA).

2.4. Magnetic Characterization

Magnetic characterization of the samples was conducted using SQUID magnetometry (MPMS3, Quantum Design, San Diego, CA, USA). The measurements included out-of-plane magnetic hysteresis loops at multiple temperatures and magnetization as a function of temperature $M(T)$ curves. To enhance the signal-to-noise ratio, particularly given the small magnetic moments of these samples, the instrument was operated in vibrating sample magnetometer (VSM) mode. This setup provided improved sensitivity and reliability in detecting the magnetic properties of the Mn-doped Bi_2Te_3 thin films.

2.5. X-Ray Spectroscopy

Element-specific XMCD provides a powerful tool for probing the magnetic ground state of materials using circularly polarized X-rays [38]. Measurements at the Mn $L_{2,3}$ edge were performed on the I10 (BLADE) beamline at Diamond Light Source (Didcot, UK) at the base temperature of ∼2.5 K. A superconducting magnet was used to apply magnetic fields of up to 14 T along the incident beam direction. The X-ray absorption spectra (XAS) were recorded in total-electron yield (TEY) mode, which yields surface-sensitive information with a $1/e$ probing depth of ∼3–5 nm. The XMCD signal is provided by the difference between XAS spectra acquired with right- and left-circularly polarized light. Previously, XMCD has been successfully used to unambiguously determine the electronic and magnetic state of the magnetically active dopants in TIs [31,39–41].

3. Results

3.1. Thin Film Growth and Structural Characterization

XRD analysis of the films at room temperature confirms a Bi_2Te_3 structure with the $R\bar{3}m$ space group (Figure 1a). The Mn concentrations of the films and their general stoichiometry was determined by SEM-EDS. A summary of the produced samples is provided in Table 1. Note that the nominal Mn concentrations in Table 1 represent the ratio of growth rates for Mn and Bi_2Te_3. For the undoped sample, the calculated *c* lattice parameter is 31.4 Å. This value decreases slightly with increasing Mn concentration, reaching 31.1 and 30.6 Å at 0.8% and 6.0% Mn, respectively. However, beyond 6% Mn incorporation this behavior shifts and the *c*-lattice parameter begins to increase, reaching 31.9 and 32.3 Å at 8.5% and 11.7% Mn, respectively. This trend suggests a critical concentration beyond which the dopant exhibits behavior different from the desired substitutional doping on Bi sites, possibly occupying sites in the van der Waals gap or forming a structure akin to $MnBi_2Te_4$, where an MnTe bilayer is incorporated in the joint unit cell with Bi_2Te_3 unit cell. Additionally, extra peaks can be seen where the intensity increases as the doping concentration increases, suggesting the formation of secondary phases within the doped Bi_2Te_3 matrix.

As standard XRD primarily probes crystal structures in the *c*-plane, GI-XRD was used to investigate off-axis structures. GI-XRD has a fixed incidence angle, allowing it to reveal the presence of $MnTe_x$ phases within the films (Figure 1b). These secondary peaks, while inconsistent across samples, align with $MnTe_x$ diffraction patterns, suggesting random orientation of $MnTe_x$ growth within the films. This randomness aligns with the granular growth characteristic of magnetron-sputtered thin films and further supports the hypothesis of secondary phase formation at higher Mn concentrations.

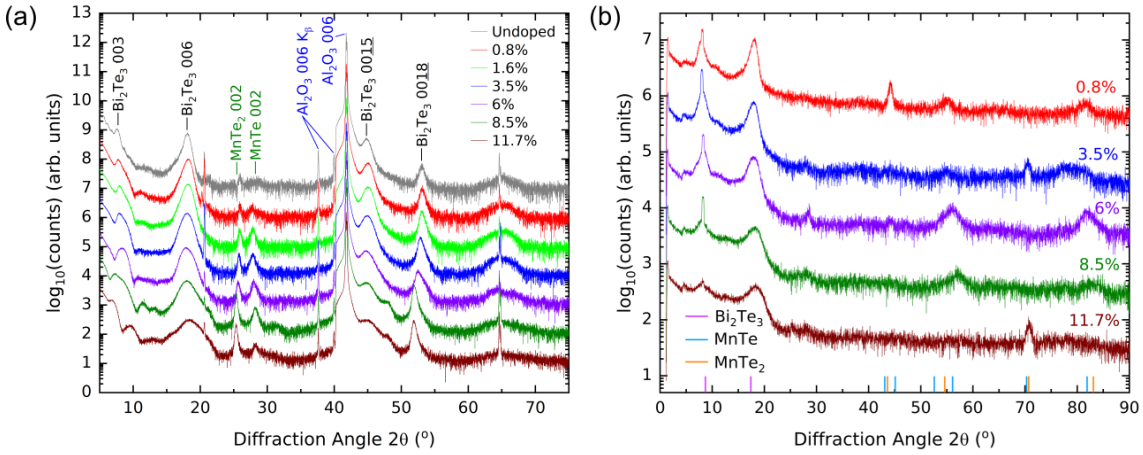

Figure 1. (**a**) X-ray diffraction patterns of Mn-doped Bi_2Te_3 thin films with increasing doping concentration (from top to bottom; offset for clarity). The primary Bi_2Te_3 and Al_2O_3 substrate peaks are prominent, but secondary peaks are also visible, likely corresponding to $MnTe_x$ *c*-plane reflections. These secondary peaks are challenging to identify due to overlapping peaks and minor peak shifts from lattice mismatch with the substrate. However, their relative intensities increase with increasing Mn concentration compared to the Bi_2Te_3 (00*l*) peaks. (**b**) GI-XRD patterns for the Mn:Bi_2Te_3 doping series, revealing diffraction peaks corresponding to crystal planes that are not parallel to the *c*-plane. The positions of peaks corresponding to Bi_2Te_3, MnTe, and $MnTe_2$ are indicated above the *x*-axis. The lack of consistent secondary peaks across all Mn concentrations suggests that $MnTe_x$ grows with varying preferred orientations in the different films.

Table 1. SEM-EDS analysis of the chemical composition for the series of Mn-doped Bi_2Te_3 thin films. The nominal Mn concentrations represent the ratio of growth rates for Mn and Bi_2Te_3. At low concentrations, the measured Mn incorporation into the film closely follows the nominal values. However, at concentrations exceeding ∼5%, a reduced fraction of Mn is incorporated into the films. Note that the two 3.5% films were produced using different methods: (1) by lowering the Mn power, and (2) by pulsed deposition (via periodic shuttering) at twice the power. These methods demonstrate that similar Mn concentrations can be achieved within the margin of error of the EDS measurements.

Nominal Mn Concentration (at. %)	Measured Mn Concentration (at. %)	Measured Bi Concentration (at. %)	Measured Te Concentration (at. %)
0.8	0.8 ± 0.1	38.7 ± 0.4	58.8 ± 0.5
1.7	1.6 ± 0.1	40.1 ± 0.4	58.3 ± 0.5
3.5—low power	3.5 ± 0.4	39.5 ± 0.2	57.0 ± 0.3
3.5—pulsed	3.8 ± 0.3	38.4 ± 0.1	56.8 ± 0.1
7.0	6.0 ± 0.5	38.0 ± 0.5	56.0 ± 0.5
10.6	8.5 ± 0.1	38.2 ± 1.0	53.4 ± 1.0
17.7	11.7 ± 0.1	36.7 ± 0.1	51.6 ± 0.1

To gain deeper insights into the effects of Mn doping on the crystal structure and the formation of secondary phases, RSMs were acquired over χ and 2θ ranging from $-5°$ to $65°$ and from $0°$ to $100°$, respectively. The resulting RSM plots are presented in Figures 2 and 3. Analysis of these plots confirms the appearance of additional peaks with increasing Mn concentration, consistent with the presence of $MnTe_x$ within the samples at higher doping levels. These findings corroborate the hypothesis of secondary phase formation as the Mn concentration exceeds a critical threshold, further supporting the observations from the grazing-incidence XRD data.

Reciprocal space mapping in the Q_x–Q_z plane was carried out by scanning the ω and $2\theta/\omega$ axes. The plots for four samples are shown in Figure 3. Analysis of the full width at

half maximum (FWHM) of the peaks reveals a general broadening in both axes, predominantly along the Q_z axis. For instance, the 0.8% Mn-doped sample shows a 22% increase in peak width along Q_z, while the 6.0% Mn sample exhibits a pronounced 104% increase. This trend indicates an increase in grain size for higher Mn concentrations. Additionally, as the Mn doping crosses a threshold between 6% and 12%, the peak amplitude decreases by a factor of ∼3 and undergoes significant broadening. This sharp change in amplitude and peak shape highlights the structural breakdown of the Bi_2Te_3 phase at high doping levels, aligning with the emergence of secondary $MnTe_x$ phases observed in XRD and GI-XRD measurements.

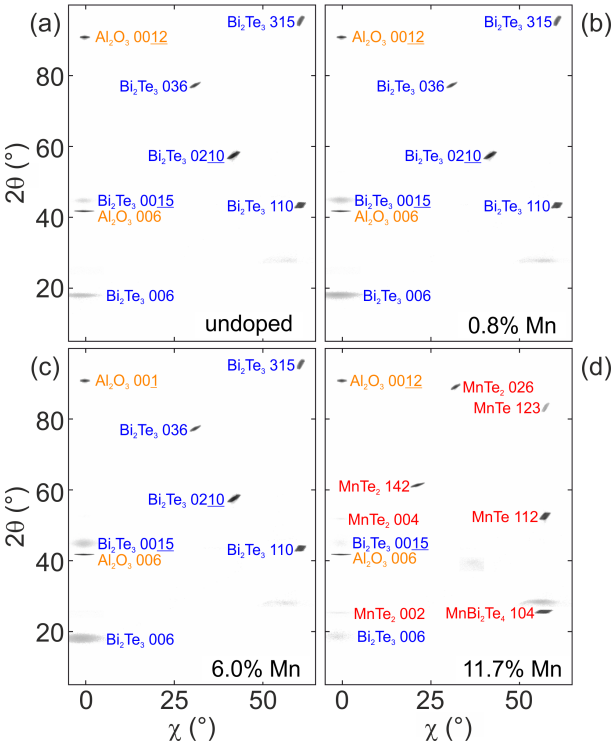

Figure 2. Asymmetric RSMs of Bi_2Te_3 thin films at various Mn doping levels: (**a**) undoped, (**b**) 0.8%, (**c**) 6.0%, and (**d**) 11.7%. The undoped sample exhibits only Bi_2Te_3 and Al_2O_3 peaks. In (**b**,**c**), the secondary phase peaks that were observed in the 1D XRD measurements (Figure 1) are below the detection threshold in the RSM data. Broadening of the Bi_2Te_3 peaks in (**c**) suggests an increase in grain size. In (**d**), the Bi_2Te_3 peak intensity significantly decreases, with multiple peaks attributed to $MnTe_x$ and $MnBi_2Te_4$ appearing, indicating a shift in the doping mechanism at higher Mn concentrations.

To investigate the grain size and surface morphology of the films, AFM was performed. Representative images for an undoped Bi_2Te_3 thin film and a Mn-doped sample (3.5% Mn) are shown in Figure 4a and 4b, respectively. The nanocrystalline nature of the film is evident, with no clear anisotropy in grain orientation observed in either samples. The introduction of Mn significantly alters the surface morphology, resulting in increased roughness and larger grain sizes compared to the undoped film. Grain size analysis was conducted by setting a threshold depth of 5 nm and analyzing the top layer of grains. Two distinct grain size distributions were identified, i.e., grains measuring 60–70 nm and 110–120 nm across. These findings support the conclusion from XRD that multiple growth modes are present within the doped films, likely reflecting variations in Mn distribution between the two different grain types. In contrast, the undoped Bi_2Te_3 sample grown under the same conditions exhibits significantly smaller grain sizes. This indicates that Mn doping influences the growth mode even at low concentrations, potentially enhancing grain coalescence and promoting clustering. Grain boundaries are localized regions of strain and

disorder; as such, they play a significant role in influencing magnetic coupling. A reduction in their density in films with larger grains could lead to notable modifications in magnetic interactions. Future studies will focus on exploring how these morphological changes affect magnetic coupling, with particular emphasis on the transition between ferromagnetic and antiferromagnetic behavior.

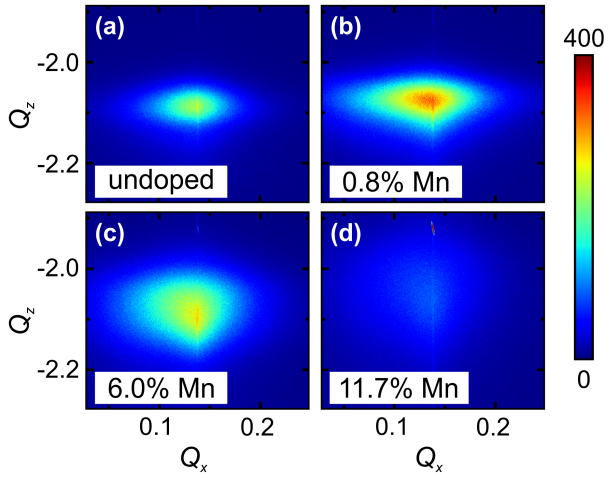

Figure 3. RSMs of the (006) peak for Bi_2Te_3 films at various Mn doping levels: (**a**) undoped, (**b**) 0.8%, (**c**) 6.0%, and (**d**) 11.7%. Peak broadening in both the Q_x and Q_z directions is observed as the Mn concentration increases to 6.0%, indicating structural changes such as increased lattice distortion and reduced crystalline coherence. In (**d**), the 11.7% doped sample shows a significant loss of intensity, suggesting a transition from substitutional doping to a structure resembling $MnBi_2Te_4$. These results align with observations from *c*-plane XRD, confirming a doping-dependent shift in film properties.

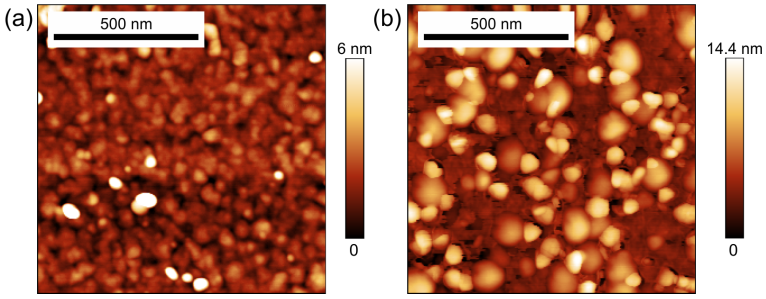

Figure 4. AFM images of (**a**) an undoped Bi_2Te_3 thin film and (**b**) a 3.5% Mn-doped sample. The dopant introduces significant changes to the surface morphology, with increased roughness and larger grain sizes. The grain size distribution was analyzed by setting the threshold to 5 nm. Two dominant grain sizes of 60–70 and 110–120 nm were observed. These distinct grain sizes suggest the presence of multiple growth modes within the film.

3.2. Electron Microscopy

STEM EDS elemental mapping was used to investigate the spatial distribution and incorporation of Mn dopants in Bi_2Te_3 thin films, while HAADF-STEM imaging provided insights into the film's structure. Note that determining the spatial distribution of Mn dopants at the nanoscale in the Bi_2Te_3 film is challenging due to the low atomic number (Z) of Mn (25) compared to Bi (83) and Te (52) as well as to the low overall concentration of Mn in the film. This makes direct imaging of Mn dopants at atomic resolution using Z-contrast in HAADF-STEM particularly difficult.

Cross-sectional STEM images, shown in Figures 5 and 6 for nominal Mn concentrations of 1.6% and 3.8%, respectively, confirm that the films are composed of oriented grains and exhibit the characteristic quintuple-layer structure of Bi_2Te_3, indicating a high degree

of order within the grains. In principle, these observations underscore the successful integration of Mn into the Bi_2Te_3 matrix without compromising the layered structure, consistent with conclusions drawn from the XRD analysis.

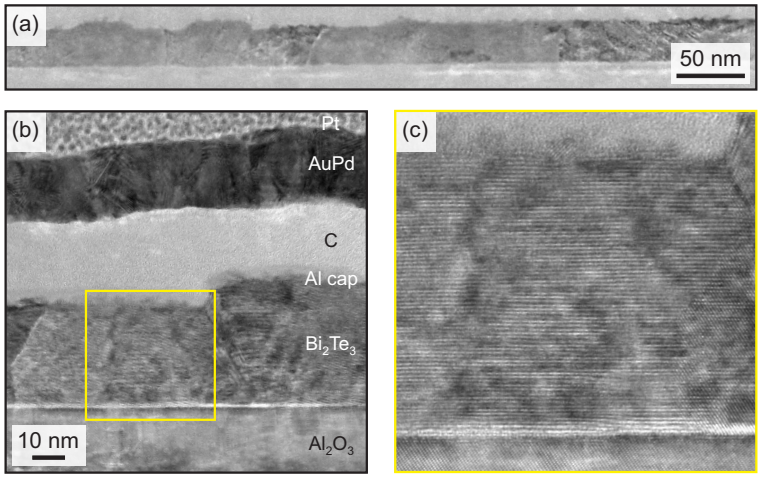

Figure 5. BF-TEM images of a Bi_2Te_3 film doped with 1.6% Mn. (**a**) Cross-sectional view of the film, showing the surface roughness. (**b**) Image of the full film stack, including protective layers of C, AuPd, and Pt required for the specimen preparation. Roughness and discontinuities in the *c*-plane-aligned layers are visible, particularly to the right of the highlighted section. (**c**) The magnified view of the highlighted area in (**b**) reveals individual Bi_2Te_3 quintuple layers, demonstrating that the film is textured and *c*-axis oriented.

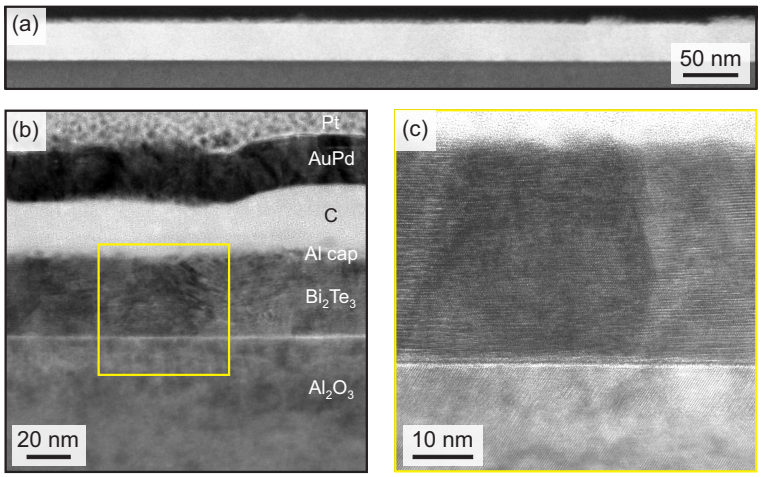

Figure 6. BF-TEM images of a Bi_2Te_3 thin film with 3.8% Mn. (**a**) Cross-sectional view of the film, showing a reduced roughness compared to the 1.6% Mn film. (**b**) Image showing the full stack including the protective layers needed for preparation. The highlighted section indicates the area magnified in (**c**) and shows evidence of off-axis growth. (**c**) Enlarged view of the locally disordered quintuple layer stack. A significant area of off-axis growth is observed, suggesting the potential formation of a crystal structure with a different space group than Bi_2Te_3.

The HAADF-STEM overviews for the two concentrations shown in Figure 7a,d reveal the characteristic (quintuple) layer structure of the Bi_2Te_3 film. Upon closer inspection, the HAADF-STEM image intensity is found to vary across the film, with patches of lower intensity (dark areas) interspersed throughout. Brighter areas correspond to Mn-rich regions, while darker areas indicate Mn-poor regions. These variations suggest compositional differences, possibly due to a non-uniform distribution of Mn dopants.

To test this hypothesis, EDS spectra were collected from both light and dark regions of the film in the 1.6% Mn-doped sample shown in Figure 7g. The Mn peak at 5.9 keV

was integrated and normalized to the total spectral integral, accounting for possible co-dependencies with other elemental peaks. This analysis revealed that the Mn content in the bright regions is ∼35% higher than in the darker regions, confirming significant compositional heterogeneity. To further analyze the extent of Mn-rich areas, grayscale HAADF images were thresholded based on brightness and the relative areas of bright (Mn-rich) and dark (Mn-poor) regions were calculated. Across multiple images at varying magnifications, it was determined that ∼68% of the film consists of Mn-rich regions, with the remaining 32% being Mn-poor. This uneven distribution is consistent with the XRD and GI-XRD findings, which suggest the presence of $MnTe_x$ secondary phases.

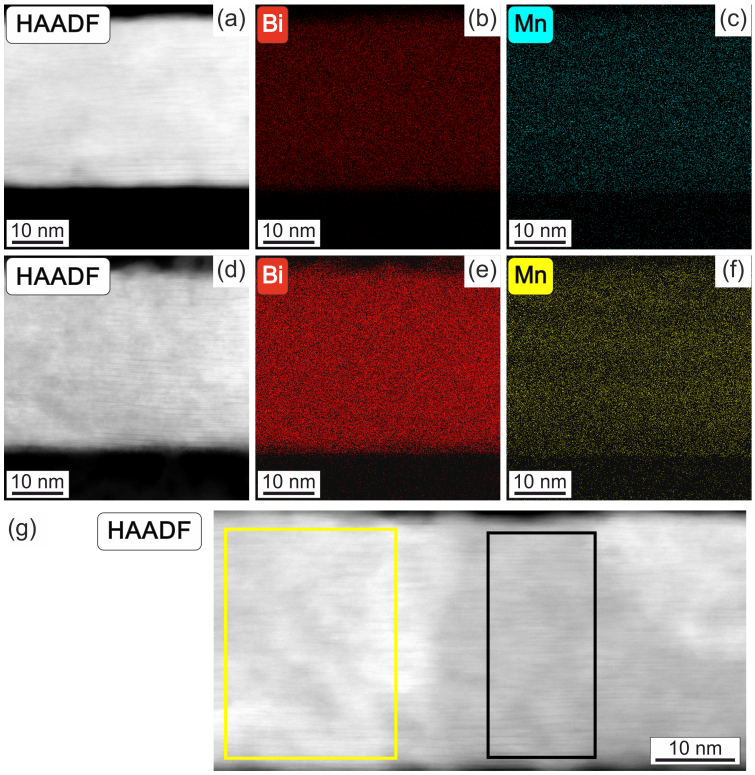

Figure 7. (**a**) HAADF-STEM image of a Bi_2Te_3 thin film doped with 1.6% Mn. Light and dark regions are visible across the *c*-axis-orientated layers. This indicates compositional variation, as the signal intensity depends on atomic number. (**b**,**c**) Corresponding STEM EDS maps for Bi and Mn, respectively. (**d**) HAADF-STEM image of a Bi_2Te_3 thin film doped with 3.8% Mn, showing similar light and dark regions. (**e**,**f**) Corresponding EDS maps for Bi and Mn for the 3.8% Mn sample. (**g**) While Mn appears evenly distributed in the EDS images, statistical analysis of the Mn peak intensities normalized by the total spectral integral reveals that the lighter region (yellow rectangle) contain 35% more Mn than the darker region (black rectangle).

Figure 7e,f provides further elemental mapping for the 3.8% Mn film, showing that Mn is distributed across both the bright and dark regions, though most likely in differing concentrations. Combined with structural data, these findings suggest that the Mn-rich regions consist of a mixture of substitutionally doped Bi_2Te_3 and $MnTe_x$ secondary phases. The consistent Bi content observed in EDS maps supports the hypothesis that Bi_2Te_3 remains the dominant matrix, with Mn integrated as either a substitutional dopant or as part of secondary phases.

3.3. Magnetic Characterization

Vibrating-sample SQUID magnetometry was performed as a function of both temperature and applied magnetic field (up to 5 T). The sample surface was oriented perpendicular to the applied magnetic field. The resulting magnetic hysteresis loop for a film with an Mn

concentration of 3.8% is shown in Figure 8a, indicating soft ferromagnetic behavior with a coercive field of approximately 36 mT at 5 K. After subtracting the diamagnetic contribution of the sapphire substrate, the data reveal a strong paramagnetic-like contribution which does not reach full saturation within the instrumental field range of 5 T, necessitating higher fields. The overall shape of the hysteresis loop is generally similar to that of MBE-grown $Mn_xBi_{2-x}Te_3$ films reported in previous studies [42,43]. The combination of low coercivity and paramagnetic-like behavior is attributed to the continuous reorientation of magnetic domains under the applied field [42,43].

To determine the T_C of the films, $M(T)$ curves were measured from 5 to 300 K. First-order derivatives of these curves for samples with Mn concentrations of 3.8% and 11.7% are shown in Figure 8c and 8d, respectively. These derivatives reveal two distinct magnetic transitions as the temperature increases from 5 K, one at ∼10 K and another at ∼43.3 K. Given the XRD evidence of $MnTe_x$ secondary phases in the films, these transitions are likely associated with the distinct contributions of Mn in different environments. The most likely scenario is that the lower-temperature transition (∼10 K) is attributed to the ferromagnetic order of Mn substitutionally doped into the Bi_2Te_3 lattice, while the higher-temperature transition (∼43.3 K) corresponds to magnetic ordering within the $MnTe_x$ phase.

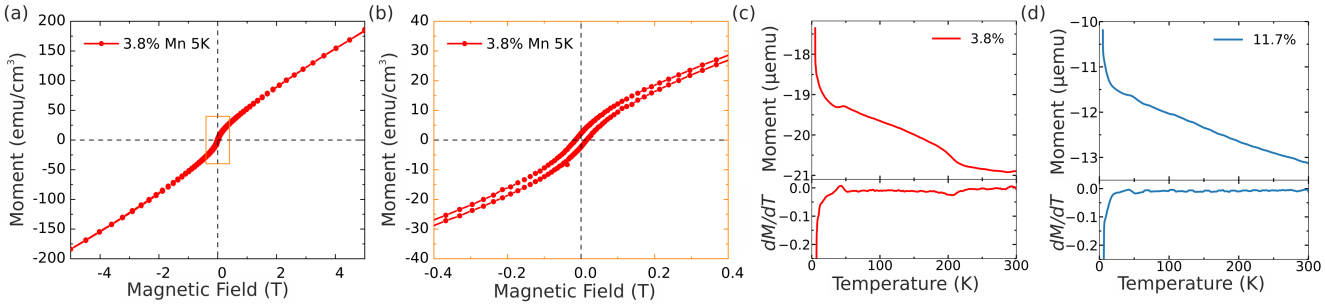

Figure 8. Magnetic characterization of Mn-doped Bi_2Te_3 thin films. (**a**) Magnetization versus magnetic field ($M(H)$) hysteresis loop of a sample with 3.8% Mn doping measured at 5 K. (**b**) Magnified view of the highlighted region (orange) in (**a**), showing detailed low-field behavior. (**c**,**d**) Temperature-dependent magnetization ($M(T)$) plots for samples with 3.8% and 11.7% Mn doping, respectively, with the derivative dM/dT shown below each plot. Discontinuities in dM/dT reveal magnetic transitions at approximately 10 K and 43 K. These transition temperatures are consistent with the presence of two magnetic phases in the films, as suggested by the structural analysis.

3.4. X-Ray Spectroscopy

XMCD was employed to investigate the magnetic ground state of the Mn-doped Bi_2Te_3 thin films. The element-specific capability of XMCD allows for probing the magnetic contribution of Mn dopants within a TI matrix. Measurements were conducted at the base temperature of ∼2.5 K in magnetic fields of up to 14 T along the incident beam direction, ensuring magnetic saturation of the films. The films were oriented normal to the beam, allowing for probing of magnetic moments aligned out-of-plane relative to the film surface.

Figure 9a presents the XMCD spectra for films with varying Mn concentrations normalized to the maximum at the L_3 edge of the XAS spectra summed over both polarizations. Consistent with previous results on MBE-grown Mn-doped TIs, pronounced dichroism is observed [42,44]. However, as the Mn concentration increases, the XMCD peak intensity decreases, indicating that only a subset of Mn ions contributes to the ferromagnetic order. The remaining Mn ions contribute to the total XAS intensity, but not to the dichroism.

To quantify this, the L_3 edge peak asymmetry was analyzed. The peak asymmetry, defined as the difference between the XAS spectra for opposite circular polarizations divided by their sum, is proportional to the spin magnetic moment of Mn in the film [45,46]. The asymmetry was calculated for five samples and plotted against the Mn concentration

in Figure 9d. The results reveal a linear reduction in asymmetry (and consequently in the moment per Mn atom) with increasing Mn doping, with the asymmetry approaching zero at higher concentrations.

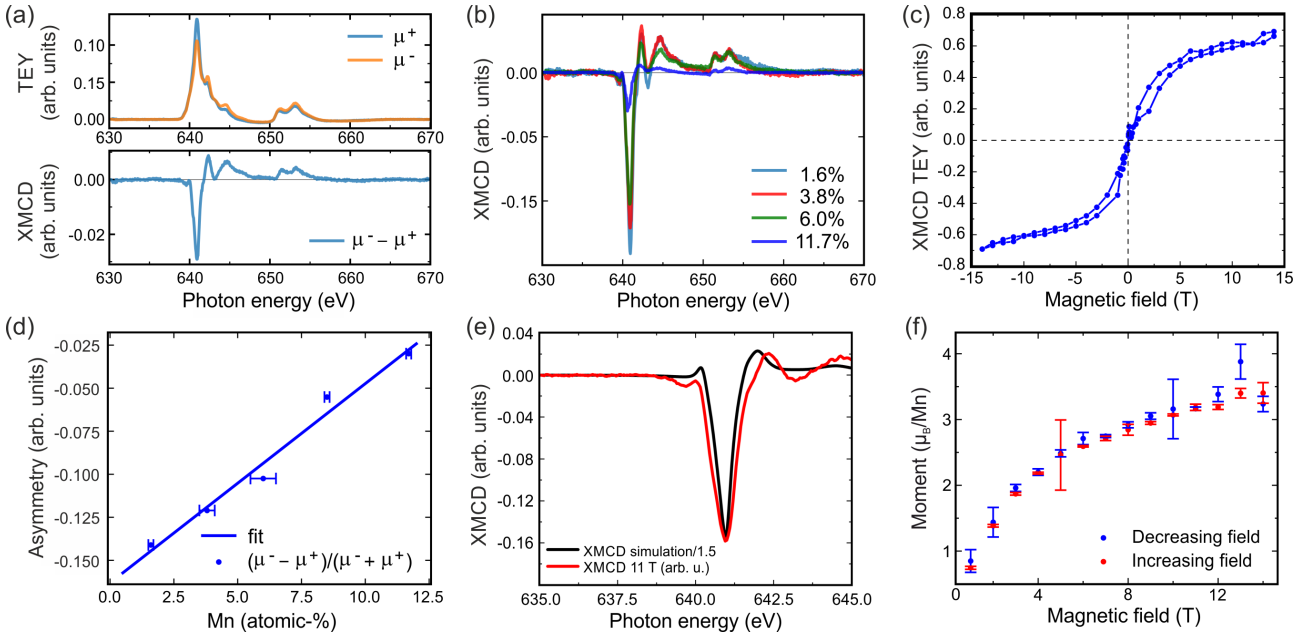

Figure 9. X-ray magnetic circular dichroism (XMCD) analysis of Mn-doped Bi_2Te_3 thin films. (**a**) XAS (top) and XMCD (bottom) spectra at the $L_{2,3}$ edges for a thin film with 3.8% Mn doping at normal incidence under a 1 T applied field parallel to the beam, showing pronounced dichroism. (**b**) XMCD spectra for a series of doped samples, normalized by the maximum of the XAS sum at the L_3 edge. The XMCD intensity decreases with increasing Mn concentration. (**c**) XMCD hysteresis curve for a Bi_2Te_3 film with 6% Mn, illustrating magnetic behavior as a function of applied field. (**d**) Plot of peak asymmetry versus atomic-% Mn, highlighting the reduction in magnetic moment (per Mn) with increasing Mn doping, as observed in (**b**). (**e**) XMCD spectrum at the L_3 edge under an 11 T applied field (to ensure saturation) compared with the simulated spectrum for an Mn site in Bi_2Se_3. (**f**) Magnetic moment per Mn atom as a function of the applied field, calculated from the XMCD hysteresis loop in (**c**) and scaled using the simulated spectra in (**e**). The saturation moment is $\sim(3.48 \pm 0.25)\ \mu_B$/Mn.

Due to photon energy-dependent background variation as well as to L_3–L_2 peak overlap, sum rule analysis to directly extract spin and orbital moments was unreliable. However, owing to the proportionality between asymmetry and moment, the value of the Mn spin moment within the film can be determined through comparison with calculated spectra. Figure 9e shows the Mn L_3 edge from experimental data compared to a calculated spectrum generated via atomic multiplet calculations (see details in [42]). The spectra for the hybridized ground state were simulated with mixed d^4, d^5, and d^6 character, yielding a moment of 4.75 μ_B/Mn atom for a fully saturated film. This magnetic moment comparison provides a scaling factor to estimate the moment for films at high fields.

Figure 9c shows an XMCD hysteresis loop for a film with 6.0% Mn. While the loop does not explicitly demonstrate saturation, we argue in the following that the film reaches saturation at ~13 T. Using the scaling factor derived from the simulated data, the magnetic moment per Mn atom was plotted as a function of the applied field, as shown in Figure 9f. The normalized data corrected for apparent paramagnetic contributions reveal that the film becomes saturated near 13 T. From the saturated region, the average moment per Mn atom was calculated using measurements at 13 and 14 T on both the upward and downward sweeps of the hysteresis curve. This analysis yielded an average moment of $(3.48 \pm 0.25)\ \mu_B$/Mn atom for this particular Mn concentration of 6.9%.

4. Discussion

In Figure 9d, the asymmetry A as a function of the Mn concentration x (in atomic-%) is plotted and fitted with a linear function of the form $A(x) = -0.163 + 0.0116x$. This relationship implies that the magnetic moment M per Mn atom (normalized to 1 at $x = 0.0$) follows the expression $M(x) = 1 - 0.0712x$, indicating that each additional atomic-% Mn reduces the moment by a fixed amount of 0.0712. Such behavior is unconventional. Typically, $M(x)$ remains constant until all available sites within the Bi_2Te_3 lattice which are linked to ferromagnetic behavior are fully occupied, after which the moment per Mn decreases sharply as Mn begins to populate energetically unfavorable sites, resulting in either paramagnetic or antiferromagnetic behavior [10,42,43]. Thus, the observed linear reduction in $M(x)$ suggests a different mechanism.

The decrease in $M(x)$ can be attributed to several interconnected mechanisms involving substitutional Mn doping, Mn clustering, and secondary phase formation. At low Mn concentrations, substitutional doping dominates, maximizing the ferromagnetic moment [9]. However, as x increases, Mn dopants may begin to occupy less favorable positions, such as interstitial sites or van der Waals gaps, as suggested by the structural data (e.g., XRD and STEM-EDS; see Figures 1 and 7). Mn atoms in these positions could couple antiferromagnetically to substitutional Mn, reducing the measured net moment in XMCD. This behavior aligns with theoretical predictions of antiferromagnetic coupling between Mn ions in TIs [15]. Furthermore, as the Mn concentration increases, the proximity of Mn ions enhances superexchange interactions, which may lead to frustration effects in the lattice, resulting in suppressed long-range ferromagnetic ordering [8,26].

The presence of secondary phases and Mn clustering further complicates the magnetic behavior. Mn dopants may cluster at higher concentrations due to limited mobility during sputtering growth, as supported by our HAADF-STEM observations (Figure 7). Such clustering could introduce regions with local antiferromagnetic interactions, reducing the overall ferromagnetic response [42]. In addition, the emergence of $MnTe_x$ phases, evidenced by GI-XRD (Figure 1b), introduces nonmagnetic or weakly magnetic regions that do not contribute to the ferromagnetic order of the substitutional Mn ions [17].

Strain-induced effects may also play a significant role. Increasing Mn concentration can introduce local lattice strain or disorder, as indicated by the broadening of XRD and RSM peaks (Figures 2 and 3). Strain modifies the local magnetic exchange interactions and may weaken ferromagnetic coupling in the lattice [43]. Additionally, Mn doping introduces carriers, likely holes, which mediate the exchange interaction between Mn spins. At higher Mn concentrations, the carrier-mediated interaction could transition to favor antiferromagnetic or spin-glass behavior, suppressing the net ferromagnetic response [47]. Changes in the host Bi_2Te_3 electronic structure, such as band structure modifications and surface state degradation, may further weaken magnetic ordering [34].

The observation that the lowest Mn doping data point in Figure 9d (1.6% Mn) already aligns with the linear trend observed at higher concentrations suggests that substitutional doping may have reached saturation even at this low concentration, likely as a result of the specific growth mode employed. During magnetron sputtering in the used configuration with two separate targets, Mn clustering may occur from the start, particularly under pulsed growth conditions. As Mn ions are incorporated, the mobility limitations (as compared to a layer-by-layer growth mode in MBE) could prevent Mn from fully occupying substitutional sites within Bi_2Te_3 clusters. This behavior could explain why Mn clustering observed in HAADF-STEM (Figure 7) and antiferromagnetic contributions appear even at low doping levels.

While these mechanisms align with the observed linear trend, further investigations are required to probe site-specific magnetic ordering and structural effects. Techniques

such as neutron diffraction, density functional theory simulations, or more extensive high-resolution electron microscopy could provide additional insights into Mn site preferences, clustering, and coupling interactions. Additionally, TEM and X-ray photoelectron spectroscopy studies could help to establish the solubility limit of Mn within Bi_2Te_3 films, enabling the reliable synthesis of films that contain only substitutionally doped Mn. Understanding this limit could enable the further optimization of growth conditions, such as tuning deposition temperatures or reducing deposition. Such combined studies would clarify the interplay between substitutional doping, secondary phase formation, and magnetic ordering, highlighting the importance of controlling growth conditions to optimize magnetic properties [47,48].

The findings presented here highlight the unique characteristics of Mn-doped Bi_2Te_3 films synthesized via magnetron sputtering, a technique with significant advantages over MBE. Unlike MBE, sputtering facilitates the growth of nanocrystalline films with scalable deposition and precise control over grain size. These features suppress bulk conduction pathways and enhance the role of surface states, which is critical for applications in spintronics.

Recent work has demonstrated that sputtered topological insulators such as BiSb and BiSe exhibit high spin Hall angles ($\theta_{SH} \approx 10$) and efficient spin–orbit torque (SOT) magnetization switching at room temperature, along with low critical current densities [32,49]. These advancements underscore the potential of sputtered films in developing ultra-low-power devices, including SOT-MRAM and racetrack memory.

While the granular structure of our Mn-doped Bi_2Te_3 films provides opportunities for tuning grain boundaries and magnetic dopant interactions, these samples are less suited for room-temperature SOT-based devices due to their specific magnetic properties. Future low-temperature magnetotransport studies could further elucidate the coupling between magnetic order and topological surface states in these films, revealing phenomena such as the quantum anomalous Hall effect.

Thus, magnetron sputtering offers a powerful platform for bridging the gap between fundamental research and industrial applications, paving the way for scalable and high-performance spintronic technologies [50–54]. Further optimization of sputtering parameters and in-depth structural and magnetic investigations will be crucial for unlocking the full potential of these materials.

5. Conclusions

This study investigated the structural and magnetic properties of nanocrystalline Mn-doped Bi_2Te_3 thin films. Structural characterization revealed the presence of $MnTe_x$ secondary phases even at low Mn concentrations. Cross-sectional EDS analysis of a sample with 3.8% Mn concentration indicated an uneven dopant distribution. This suggests clustering of the secondary phase within the film, likely driven by the granular texture characteristic of sputtered films. Despite adjustments to the growth recipe, including changes in annealing conditions, growth temperature, and reduced Mn content, the secondary phases persisted.

Magnetic measurements yielded results consistent with the structural findings, indicating a more complex system than pure Mn:Bi_2Te_3. SQUID-VSM measurements revealed two magnetic transitions at ~10 and ~43 K, suggesting distinct magnetic ordering contributions from both the doped TI and $MnTe_x$ phases. From XMCD measurements, the magnetic moment of Mn was found to be inversely proportional to the doping concentration. This trend is consistent with theoretical predictions that Mn ions at different lattice sites will exhibit varying magnetic behaviors, including antiferromagnetic coupling between Mn ions in the van der Waals gap and those substituting Bi ions [15]. Comparison with simulated XMCD data yielded an estimated average moment of $(3.48 \pm 0.25)\ \mu_B$/Mn for the sample with

6.0% Mn. Notably, this value provides the average over the magnetic and non-magnetic Mn fractions.

Comparison with previous single-crystal [44] and MBE-grown [42] Mn:Bi_2Te_3 samples highlights the challenges of achieving a single-crystalline structure in sputtered films. While this complicates interpretation, it presents an opportunity to explore the growth of the intrinsic magnetic TI $MnBi_2Te_4$. $MnBi_2Te_4$ exhibits antiferromagnetic order and supports exotic states such as the quantum anomalous Hall effect and axion insulator states [55]. Structurally, the unit cell of $MnBi_2Te_4$ consists of a Bi_2Te_3 quintuple layer and an MnTe bilayer [56]. The prominence of MnTe phases in the studied films suggests that optimizing the growth parameters could enable realization of $MnBi_2Te_4$ via magnetron sputtering.

Author Contributions: Conceptualization, T.H.; methodology, B.A., G.v.d.L., and T.H.; formal analysis, J.B. (Joshua Bibby), B.A., G.v.d.L., and T.H.; resources, S.J.H., G.v.d.L., and T.H.; data curation, J.B. (Joshua Bibby), A.S., E.H., J.B. (Jack Bollard), and B.A.; writing—original draft preparation, J.B. (Joshua Bibby), and T.H.; writing—review and editing, T.H.; visualization, J.B. (Joshua Bibby), and T.H.; supervision, A.S., G.v.d.L., and T.H.; project administration, T.H.; funding acquisition, T.H. All authors have read and agreed to the published version of the manuscript.

Funding: The XMCD experiments were carried out on beamline I10 at Diamond Light Source (Didcot, UK) under proposal MM32078. Financial support from the Leverhulme Trust (RPG-2020-358), the John Fell Fund (University of Oxford), the Oxford-ShanghaiTech collaboration project, and the UK Skyrmion Project (Engineering and Physical Sciences Research Council, EP/N032128/1) is gratefully acknowledged. TEM access was supported by the Henry Royce Institute for Advanced Materials funded through EPSRC grants EP/R00661X/1, EP/S019367/1, EP/P025021/1, and EP/P025498/1. We acknowledge Diamond Light Source for provision of facilities in the Materials Characterisation Laboratory. J.B. (Joshua Bibby) was supported by the Leverhulme Trust (RPG-2020-358). E.H. acknowledges an STFC-Diamond-EPSRC studentship (2604894, EP/R513295/1, EP/T517811/1), and J.B. (Joshua Bibby) acknowledges a Diamond-EPSRC studentship (2606404, EP/R513295/1, EP/T517811/1).

Data Availability Statement: The data that support the findings of this study are included withing the article.

Conflicts of Interest: The authors declare no conflicts of interest.

References

1. Qi, X.L.; Hughes, T.L.; Zhang, S.C. Topological Field Theory of Time-Reversal Invariant Insulators. *Phys. Rev. B* **2008**, *78*, 195424. [CrossRef]
2. Zhang, S.C.; Zhang, H.; Liu, C.X.; Qi, X.L.; Dai, X.; Fang, Z. Topological Insulators in Bi_2Se_3, Bi_2Te_3 and Sb_2Te_3 with a Single Dirac Cone on the Surface. *Nat. Phys.* **2009**, *5*, 438–442. [CrossRef]
3. Qi, X.L.; Li, R.; Zang, J.; Zhang, S.C. Inducing a Magnetic Monopole with Topological Surface States. *Science* **2009**, *323*, 1184–1187. [CrossRef] [PubMed]
4. Hasan, M.Z.; Kane, C.L. Colloquium: Topological Insulators. *Rev. Mod. Phys.* **2010**, *82*, 3045–3067. [CrossRef]
5. Qi, X.L.; Zhang, S.C. Topological Insulators and Superconductors. *Rev. Mod. Phys.* **2011**, *83*, 1057–1110. [CrossRef]
6. Chang, C.Z.; Zhang, J.; Feng, X.; Shen, J.; Zhang, Z.; Guo, M.; Li, K.; Ou, Y.; Wei, P.; Wang, L.L.; et al. Experimental Observation of the Quantum Anomalous Hall Effect in a Magnetic Topological Insulator. *Science* **2013**, *340*, 167–170. [CrossRef]
7. Chen, Y.L.; Chu, J.H.; Analytis, J.G.; Liu, Z.K.; Igarashi, K.; Kuo, H.H.; Qi, X.L.; Mo, S.K.; Moore, R.G.; Lu, D.H.; et al. Massive Dirac Fermion on the Surface of a Magnetically Doped Topological Insulator. *Science* **2010**, *329*, 659–662. [CrossRef] [PubMed]
8. Tokura, Y.; Yasuda, K.; Tsukazaki, A. Magnetic Topological Insulators. *Nat. Rev. Phys.* **2019**, *1*, 126–143. [CrossRef]
9. Hor, Y.S.; Roushan, P.; Beidenkopf, H.; Seo, J.; Qu, D.; Checkelsky, J.G.; Wray, L.A.; Hsieh, D.; Xia, Y.; Xu, S.Y.; et al. Development of Ferromagnetism in the Doped Topological Insulator $Bi_{2-x}Mn_xTe_3$. *Phys. Rev. B* **2010**, *81*, 195203. [CrossRef]
10. Watson, M.D.; Collins-McIntyre, L.J.; Shelford, L.R.; Coldea, A.I.; Prabhakaran, D.; Speller, S.C.; Mousavi, T.; Grovenor, C.R.M.; Salman, Z.; Giblin, S.R.; et al. Study of the Structural, Electric and Magnetic Properties of Mn-Doped Bi_2Te_3 Single Crystals. *New J. Phys.* **2013**, *15*, 103016. [CrossRef]

11. Lee, J.S.; Richardella, A.; Rench, D.W.; Fraleigh, R.D.; Flanagan, T.C.; Borchers, J.A.; Tao, J.; Samarth, N. Ferromagnetism and spin-dependent transport in *n*-type Mn-doped bismuth telluride thin films. *Phys. Rev. B* **2014**, *89*, 174425. [CrossRef]
12. Ginley, T.P.; Wang, Y.; Law, S. Topological Insulator Film Growth by Molecular Beam Epitaxy: A Review. *Crystals* **2016**, *6*, 154. [CrossRef]
13. Carva, K.; Kudrnovský, J.; Máca, F.; Drchal, V.; Turek, I.; Baláž, P.; Tkáč, V.; Holý, V.; Sechovský, V.; Honolka, J. Electronic and Transport Properties of the Mn-Doped Topological Insulator Bi_2Te_3: A First-Principles Study. *Phys. Rev. B* **2016**, *93*, 214409. [CrossRef]
14. Hosokawa, S.; Stellhorn, J.R.; Matsushita, T.; Happo, N.; Kimura, K.; Hayashi, K.; Ebisu, Y.; Ozaki, T.; Ikemoto, H.; Setoyama, H.; et al. Impurity Position and Lattice Distortion in a Mn-Doped Bi_2Te_3 Topological Insulator Investigated by X-Ray Fluorescence Holography and X-Ray Absorption Fine Structure. *Phys. Rev. B* **2017**, *96*, 214207. [CrossRef]
15. Antonov, V.N.; Bekenov, L.V.; Uba, S.; Ernst, A. Electronic Structure and X-Ray Magnetic Circular Dichroism in Mn-Doped Topological Insulators Bi_2Se_3 and Bi_2Te_3. *Phys. Rev. B* **2017**, *96*, 224434. [CrossRef]
16. Zhang, D.; Richardella, A.; Rench, D.W.; Xu, S.Y.; Kandala, A.; Flanagan, T.C.; Beidenkopf, H.; Yeats, A.L.; Buckley, B.B.; Klimov, P.V.; et al. Interplay between Ferromagnetism, Surface States, and Quantum Corrections in a Magnetically Doped Topological Insulator. *Phys. Rev. B* **2012**, *86*, 205127. [CrossRef]
17. Teng, J.; Liu, N.; Li, Y. Mn-Doped Topological Insulators: A Review. *J. Semicond.* **2019**, *40*, 081507. [CrossRef]
18. Hadia, N.M.A.; Mohamed, S.H.; Mohamed, W.S.; Alzaid, M.; Khan, M.T.; Awad, M.A. Structural, optical and electrical properties of $Bi_{2-x}Mn_xTe_3$ thin films. *J. Mater. Sci. Mater. Electron.* **2022**, *33*, 158–166. [CrossRef]
19. Kander, N.S.; Biswas, S.; Guchhait, S.; Singha, T.; Das, A.K. The role of Mn in $Bi_{2-x}Mn_xTe_3$ topological insulator: Structural, compositional, magnetic, and weak anti-localization property analysis. *J. Mater. Sci. Mater. Electron.* **2023**, *34*, 1198. [CrossRef]
20. Yu, R.; Zhang, W.; Zhang, H.J.; Zhang, S.C.; Dai, X.; Fang, Z. Quantized Anomalous Hall Effect in Magnetic Topological Insulators. *Science* **2010**, *329*, 61–64. [CrossRef]
21. Zhang, J.M.; Ming, W.; Huang, Z.; Liu, G.B.; Kou, X.; Fan, Y.; Wang, K.L.; Yao, Y. Stability, Electronic, and Magnetic Properties of the Magnetically Doped Topological Insulators Bi_2Se_3, Bi_2Te_3, and Sb_2Te_3. *Phys. Rev. B* **2013**, *88*, 235131. [CrossRef]
22. Kou, X.; Lang, M.; Fan, Y.; Jiang, Y.; Nie, T.; Zhang, J.; Jiang, W.; Wang, Y.; Yao, Y.; He, L.; et al. Interplay between Different Magnetisms in Cr-Doped Topological Insulators. *ACS Nano* **2013**, *7*, 9205–9212. [CrossRef]
23. Ye, M.; Li, W.; Zhu, S.; Takeda, Y.; Saitoh, Y.; Wang, J.; Pan, H.; Nurmamat, M.; Sumida, K.; Ji, F.; et al. Carrier-Mediated Ferromagnetism in the Magnetic Topological Insulator Cr-doped $(Sb,Bi)_2Te_3$. *Nat. Commun.* **2015**, *6*, 8913. [CrossRef]
24. Tcakaev, A.; Zabolotnyy, V.B.; Green, R.J.; Peixoto, T.R.F.; Stier, F.; Dettbarn, M.; Schreyeck, S.; Winnerlein, M.; Vidal, R.C.; Schatz, S.; et al. Comparing Magnetic Ground-State Properties of the V- and Cr-Doped Topological Insulator $(Bi,Sb)_2Te_3$. *Phys. Rev. B* **2020**, *101*, 045127. [CrossRef]
25. Choi, Y.H.; Jo, N.H.; Lee, K.J.; Yoon, J.B.; You, C.Y.; Jung, M.H. Transport and Magnetic Properties of Cr-, Fe-, Cu-Doped Topological Insulators. *J. Appl. Phys.* **2011**, *109*, 07E312. [CrossRef]
26. Zhao, W.; Cortie, D.; Chen, L.; Li, Z.; Yue, Z.; Wang, X. Quantum Oscillations in Iron-Doped Single Crystals of the Topological Insulator Sb_2Te_3. *Phys. Rev. B* **2019**, *99*, 165133. [CrossRef]
27. Figueroa, A.I.; van der Laan, G.; Collins-McIntyre, L.J.; Cibin, G.; Dent, A.J.; Hesjedal, T. Local Structure and Bonding of Transition Metal Dopants in Bi_2Se_3 Topological Insulator Thin Films. *J. Phys. Chem. C* **2015**, *119*, 17344–17351. [CrossRef]
28. Abdalla, L.B.; Seixas, L.; Schmidt, T.M.; Miwa, R.H.; Fazzio, A. Topological Insulator Bi_2Se_3(111) Surface Doped with Transition Metals: An ab initio Investigation. *Phys. Rev. B* **2013**, *88*, 045312. [CrossRef]
29. Kander, N.S.; Islam, S.; Guchhait, S.; Das, A.K. The Effect of Fe-Doping on Structural, Elemental, Magnetic, and Weak Anti-Localization Properties of Bi_2Se_3 Topological Insulator. *Appl. Phys. A* **2023**, *129*, 253. [CrossRef]
30. Deng, B.; Zhang, Y.; Zhang, S.B.; Wang, Y.; He, K.; Zhu, J. Realization of Stable Ferromagnetic Order in a Topological Insulator: Codoping-Enhanced Magnetism in 4*f* Transition Metal Doped Bi_2Te_3. *Phys. Rev. B* **2016**, *94*, 054113. [CrossRef]
31. Liu, J.; Hesjedal, T. Magnetic Topological Insulator Heterostructures: A Review. *Adv. Mater.* **2023**, *35*, 2102427. [CrossRef] [PubMed]
32. DC, M.; Grassi, R.; Chen, J.Y.; Jamali, M.; Hickey, D.R.; Zhang, D.; Zhao, Z.; Li, H.; Quarterman, P.; Lv, Y.; et al. Room-Temperature High Spin-Orbit Torque due to Quantum Confinement in Sputtered $Bi_xSe_{(1-x)}$ films. *Nat. Mater.* **2018**, *17*, 800–807. [CrossRef] [PubMed]
33. Lu, Q.; Li, P.; Guo, Z.; Dong, G.; Peng, B.; Zha, X.; Min, T.; Zhou, Z.; Liu, M. Giant Tunable Spin Hall Angle in Sputtered Bi_2Se_3 Controlled by an Electric Field. *Nat. Commun.* **2022**, *13*, 1650. [CrossRef]
34. Xu, S.Y.; Neupane, M.; Liu, C.; Zhang, D.; Richardella, A.; Wray, L.A.; Alidoust, N.; Leandersson, M.; Balasubramanian, T.; Sánchez-Barriga, J.; et al. Hedgehog Spin Texture and Berry's Phase Tuning in a Magnetic Topological Insulator. *Nat. Phys.* **2012**, *8*, 616–622. [CrossRef]
35. Harrison, S.E.; Li, S.; Huo, Y.; Zhou, B.; Chen, Y.L.; Harris, J.S. Two-step growth of high quality Bi_2Te_3 thin films on Al_2O_3 (0001) by molecular beam epitaxy. *Appl. Phys. Lett.* **2013**, *102*, 171906. [CrossRef]

36. Pilidi, A.; Speliotis, T. Anomalous Hall Effect in a Magnetic Topological Insulator $(BiMn)_2Te_3$. *IEEE Trans. Magn.* **2019**, *55*, 1–6. [CrossRef]
37. Awana, G.; Fujita, R.; Frisk, A.; Chen, P.; Yao, Q.; Caruana, A.J.; Kinane, C.J.; Steinke, N.J.; Langridge, S.; Olalde-Velasco, P.; et al. Critical analysis of proximity-induced magnetism in $MnTe/Bi_2Te_3$ heterostructures. *Phys. Rev. Mater.* **2022**, *6*, 053402. [CrossRef]
38. van der Laan, G. Applications of Soft X-Ray Magnetic Dichroism. *J. Phys. Conf. Ser.* **2013**, *430*, 012127. [CrossRef]
39. Ye, M.; Eremeev, S.V.; Kuroda, K.; Krasovskii, E.E.; Chulkov, E.V.; Takeda, Y.; Saitoh, Y.; Okamoto, K.; Zhu, S.Y.; Miyamoto, K.; et al. Quasiparticle interference on the surface of Bi_2Se_3 induced by cobalt adatom in the absence of ferromagnetic ordering. *Phys. Rev. B* **2012**, *85*, 205317. [CrossRef]
40. Honolka, J.; Khajetoorians, A.A.; Sessi, V.; Wehling, T.O.; Stepanow, S.; Mi, J.L.; Iversen, B.B.; Schlenk, T.; Wiebe, J.; Brookes, N.B.; et al. In-Plane Magnetic Anisotropy of Fe Atoms on $Bi_2Se_3(111)$. *Phys. Rev. Lett.* **2012**, *108*, 256811. [CrossRef]
41. Shelford, L.R.; Hesjedal, T.; Collins-McIntyre, L.; Dhesi, S.S.; Maccherozzi, F.; van der Laan, G. Electronic structure of Fe and Co magnetic adatoms on Bi_2Te_3 surfaces. *Phys. Rev. B* **2012**, *86*, 081304. [CrossRef]
42. Collins-McIntyre, L.J.; Watson, M.D.; Baker, A.A.; Zhang, S.L.; Coldea, A.I.; Harrison, S.E.; Pushp, A.; Kellock, A.J.; Parkin, S.S.P.; van der Laan, G.; et al. X-Ray Magnetic Spectroscopy of MBE-Grown Mn-Doped Bi_2Se_3 Thin Films. *AIP Adv.* **2014**, *4*, 127136. [CrossRef]
43. Choi, Y.H.; Jo, N.H.; Lee, K.J.; Lee, H.W.; Jo, Y.H.; Kajino, J.; Takabatake, T.; Ko, K.T.; Park, J.H.; Jung, M.H. Simple Tuning of Carrier Type in Topological Insulator Bi_2Se_3 by Mn Doping. *Appl. Phys. Lett.* **2012**, *101*, 152103. [CrossRef]
44. Collins-McIntyre, L.J.; Harrison, S.E.; Schönherr, P.; Steinke, N.J.; Kinane, C.J.; Charlton, T.R.; Alba-Veneroa, D.; Pushp, A.; Kellock, A.J.; Parkin, S.S.P.; et al. Magnetic Ordering in Cr-Doped Bi_2Se_3 Thin Films. *Europhys. Lett.* **2014**, *107*, 57009. [CrossRef]
45. Thole, B.T.; Carra, P.; Sette, F.; van der Laan, G. X-ray circular dichroism as a probe of orbital magnetization. *Phys. Rev. Lett.* **1992**, *68*, 1943–1946. [CrossRef]
46. van der Laan, G.; Figueroa, A.I. X-ray magnetic circular dichroism—A versatile tool to study magnetism. *Coord. Chem. Rev.* **2014**, *277–278*, 95–129. [CrossRef]
47. Figueroa, A.I.; Hesjedal, T.; Steinke, N.J. Magnetic order in 3D topological insulators—Wishful thinking or gateway to emergent quantum effects? *Appl. Phys. Lett.* **2020**, *117*, 150502. [CrossRef]
48. Steinke, N.J.; Zhang, S.L.; Baker, P.J.; Duffy, L.B.; Kronast, F.; Krieger, J.; Salman, Z.; Prokscha, T.; Suter, A.; Langridge, S.; et al. Magnetic correlations in the magnetic topological insulator $(Cr,Sb)_2Te_3$. *Phys. Rev. B* **2022**, *106*, 224425. [CrossRef]
49. Fan, T.; Khang, N.H.D.; Nakano, S.; Hai, P.N. Ultrahigh efficient spin orbit torque magnetization switching in fully sputtered topological insulator and ferromagnet multilayers. *Sci. Rep.* **2022**, *12*, 2998. [CrossRef]
50. Yue, C.; Jiang, S.; Zhu, H.; Chen, L.; Sun, Q.; Zhang, D.W. Device Applications of Synthetic Topological Insulator Nanostructures. *Electronics* **2018**, *7*, 225. [CrossRef]
51. Gilbert, M.J. Topological electronics. *Commun. Phys.* **2021**, *4*, 70. [CrossRef]
52. Breunig, O.; Ando, Y. Opportunities in topological insulator devices. *Nat. Rev. Phys.* **2022**, *4*, 184–193. [CrossRef]
53. Kumar, P.; Kumar, R.; Kumar, S.; Khanna, M.K.; Kumar, R.; Kumar, V.; Gupta, A. Interacting with Futuristic Topological Quantum Materials: A Potential Candidate for Spintronics Devices. *Magnetochemistry* **2023**, *9*, 73. [CrossRef]
54. Jin, K.H.; Jiang, W.; Sethi, G.; Liu, F. Topological quantum devices: A review. *Nanoscale* **2023**, *15*, 12787–12817. [CrossRef]
55. Zhang, D.; Shi, M.; Zhu, T.; Xing, D.; Zhang, H.; Wang, J. Topological Axion States in the Magnetic Insulator $MnBi_2Te_4$ with the Quantized Magnetoelectric Effect. *Phys. Rev. Lett.* **2019**, *122*, 206401. [CrossRef]
56. Li, J.; Li, Y.; Du, S.; Wang, Z.; Gu, B.L.; Zhang, S.C.; He, K.; Duan, W.; Xu, Y. Intrinsic Magnetic Topological Insulators in van der Waals Layered $MnBi_2Te_4$-Family Materials. *Sci. Adv.* **2024**, *5*, 5685. [CrossRef]

Disclaimer/Publisher's Note: The statements, opinions and data contained in all publications are solely those of the individual author(s) and contributor(s) and not of MDPI and/or the editor(s). MDPI and/or the editor(s) disclaim responsibility for any injury to people or property resulting from any ideas, methods, instructions or products referred to in the content.